Platinum nanoworms self-assemble on β-cyclodextrin polymer inclusion complexes functionalized reduced graphene oxide as enhanced catalyst for direct methanol fuel cells

CrossMark

Ming Chen, Yang Meng, Jun Zhou, Guowang Diao*

College of Chemistry and Chemical Engineering, Yangzhou University, Yangzhou 225002, PR China

HIGHLIGHTS

- PtNWs/pATP-β-CDP/rGO composites are fabricated by self-assembly strategy.
- Amount and dispersity of PtNWs on rGO can be adjusted by changing the weight ratio of pATP-β-CDP/rGO.
- The catalyst displays excellent catalytic performance for methanol oxidation reaction.
- The proposed strategy provides a facile method for developing noble metals electrocatalysts.

ARTICLE INFO

ABSTRACT

A noble Pt nanoworms (PtNWs)/p-aminothiophenol (pATP)-β-cyclodextrin polymer (β-CDP)/reduced graphene oxide (PtNWs/pATP-β-CDP/rGO) nanocomposite is synthesized using the self-assembly strategy. Inclusion complexes between β-CDP and pATP are modified onto the surface of rGO through non-covalent bond force. Then, pre-prepared PtNWs self-assemble onto the surface of pATP-β-CDP/rGO through thiol and amino groups of pATP to fabricate PtNWs/pATP-β-CDP/rGO hybrid materials. It is verified that the PtNWs may be uniformly scattered on rGO and the amount of PtNWs may be adjusted changing the weight ratio of pATP-β-CDP:rGO. Cyclic voltammograms show that the PtNWs/pATP-β-CDP/rGO catalysts have higher active surface area, more improved performance and better stability towards the electrocatalytic oxidation of methanol than commercial Pt/C catalysts. The proposed synthesis strategy provides a moderate, feasible and effective method for developing noble metals electrocatalysts for methanol oxidation reaction.

© 2014 Published by Elsevier B.V.

1. Introduction

In order to tackle the daunting problem of energy dilemma and environmental pollution, scientists are searching alternative energy sources. Direct methanol fuel cells (DMFCs) are regarded as a high-efficiency, low-emission, and relatively inexpensive green energy by direct conversion of methanol fuel [1—3]. However, the low catalytic activity of electrodes for the methanol oxidation reaction has hindered the application of DMFCs. Therefore, it is of great importance to develop high active catalysts and stable electrodes for attaining high efficiency in DMFCs.

Until now, Pt or Pt alloy are the common electro-catalysts for DMFCs [4—6]. The anchoring and dispersion of Pt or Pt alloy

nanoparticles on carbon-support directly affect the catalytic activity and life. In order to load catalyst nanoparticles on the surface of carbon-support, carbon nanomaterials require a surface activation process, for example refluxing in concentrated mixtures of HNO_3 and H_2SO_4 [7—9]. However, these surface activation processes will destroy the intrinsic properties of materials, such as electrical conductivity and thermal and mechanical properties, and meanwhile cause the defects on the carbon nanomaterials. The surface defects on the carbon nanomaterials may reduce the electrochemical active surface area of catalysts and affect their durability during fuel cell operation. A moderate approach-self-assembly strategy, has attracted widely attention because it could maintain the surface activation and intrinsic property of carbon nano-materials [10—13]. Additionally, self-assembly method may also control the density and dispersion of nanoparticles on the surface of carbon nanomaterials, even anchor various kinds of nano-particles on one kind of carbon nanomaterial.

---

* Corresponding author. Tel.: +86 514 87975436; fax: +86 514 87975244.
E-mail address: gwdiao@yzu.edu.cn (G. Diao).

Carbon materials, such as carbon nanotubes [14], carbon nanofiber [15], mesoporous carbon [16,17], SiC@C [18], are currently being considered as suitable supports for catalysts in DMFCs, because of their excellent electrical conductivity, high specific surface area, and unique graphite properties. Recently, graphene nanosheet (GN) has attracted considerable attention due to its extraordinary electronic, thermal, mechanical and chemical properties [19–23]. Preparations of Pt or Pt alloy/GN hybrid materials have been widely reported [24–28]. Pt or Pt alloy/GN hybrid materials have been fabricated through two different methods, including in situ growth method [25,27,28] and self-assembly method. However, Pt or Pt alloy nanoparticles prepared from the in situ growth method lack the desired composition, dispersity and size controls, and as a result, their catalytic performance may not be fully realized. Compared with in situ growth method, it is still a challenge to realize the self-assembly of metal nanoparticles with different property, size, composition, dispersity on graphene oxide (GO) or GN.

In this study, on the basis of the self-assembly strategy, p-aminothiophenol (pATP)-β-cyclodextrin polymer (β-CDP) complex inclusion functionalized reduced graphene oxide (rGO) was prepared. Then, Pt nanoworms self-assembled on the surface of pATP-β-CDP/rGO to fabricate PtNWs/pATP-β-CDP/rGO nanocomposites. We explored the electrocatalysis of the methanol oxidation on PtNWs/pATP-β-CDP/rGO hybrid materials. We demonstrated that the new electrocatalysts have good activity and improved stability.

2. Experimental section

2.1. Materials

Natural graphite powder (99.99%) was obtained from Sigma–Aldrich (USA). β-Cyclodextrin (β-CD), p-aminothiophenol (pATP), hydrazine hydrate, K_2PtCl_6, sodium borohydride ($NaBH_4$), sodium citrate, commercial Pt/C catalyst (20% Pt), epichlorohydrin, NaOH, methanol, and concentrated H_2SO_4 (98%) were purchased from Sinopharm Chemical Reagents Company (Shanghai, China). Deionized water was used to prepare all solution.

2.2. Characterization

Ultraviolet–visible (UV–vis) absorption spectra were measured on a UV-2550 PC UV–visible spectrometer (Shimadzu, Japan). Fourier Transform infrared (FT-IR) spectra for the various samples were recorded on a Bruker Tensor 27. TEM (Transmission Electron Microscopy) observation was conducted on a Philips TECNAI-12 instrument. The Energy-dispersive X-ray (EDX) analysis was performed on a KEVEX X-ray energy detector. Diffraction (XRD) data were obtained with a graphite monochromator and Cu Kα radiation ($\lambda = 0.1541$ nm) on a D8 advance superspeed powder diffractometer (Bruker). The Raman measurements were carried out on a Raman system (Renishaw, Renishaw inVia). Carefully weighed quantities of the different samples were subjected to TGA on a STA409PC (NETZSCH) TGA instrument at a heating rate of $10\ ^\circ C\ min^{-1}$ under vacuum from 30 to 600 $^\circ C$.

All electrochemical experiments were operated with a CHI660c electrochemical workstation (Chenghua, China) with a three-electrode system including a glass carbon electrode (GCE) ($d = 3$ mm) as the working electrode, a Pt wire electrode as the counter electrode, a saturated calomel electrode (SCE) as the reference electrode. PtNWs/β-CDP-pATP/rGO, β-CDP-pATP/rGO and rGO were dispersed in deionized water to prepare the suspensions (0.5 mg mL^{-1}). The suspensions (10 μL) were spread on the surface of glass carbon disk electrodes. The coating was dried in air at room temperature to obtain the three modified electrodes.
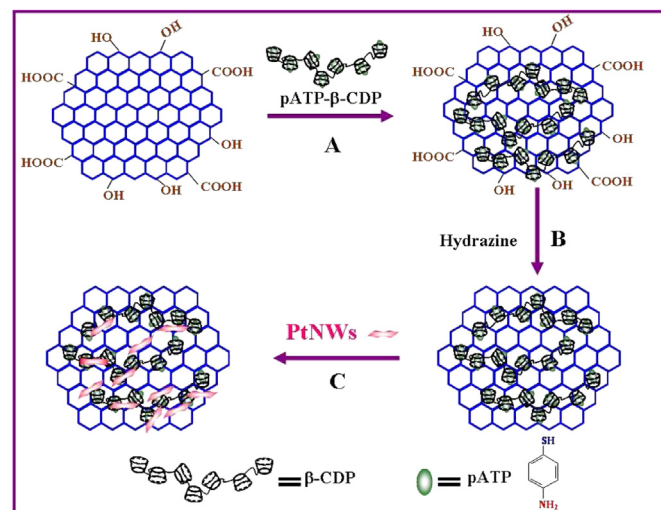
2.3. Preparation of PtNWs/pATP-β-CDP/rGO

Scheme 1 shows the strategy for the preparation of PtNWs/pATP-β-CDP/rGO via a three-step process. Firstly, water-soluble inclusion complexes of pATP-β-CDP are modified on rGO. Graphene oxide (GO) was synthesized from graphite powder using Hummer's method. β-CDP was synthesized by previously reported methods [29]. Inclusion complexes of pATP-β-CDP were prepared following the literature [30]. Then, as shown in Scheme 1A, in a typical procedure, 50 mg GO was dispersed in 10 mL deionized water by sonicating, followed by the addition of inclusion complexes (IC) with different weight ratio of IC/GO ($\gamma_{IC/G}$): 0.05, 0.1, 0.5, and then the mixtures were allowed to stir for 12 h at room temperature. Secondly, as shown in Scheme 1B, pATP-β-CDP/GO was reduced into pATP-β-CDP/rGO by hydrazine hydrate. The mixtures of pATP-β-CDP/GO were added 100 μL hydrazine hydrate and 200 μL ammonia solution and stirred vigorously at 80 $^\circ C$ for 12 h. Then, the black suspensions was separated by centrifuging and washed with deionized water three times to obtain pATP-β-CDP/rGO. Lastly, pre-synthesized PtNWs self-assemble onto pATP-β-CDP/rGO to synthesize PtNWs/pATP-β-CDP/rGO nanocomposites. Pt NWs were synthesized according to literature procedure with a slight modification. In brief, a sodium citrate solution (0.5 M, 0.5 mL) was mixed with a K_2PtCl_6 solution (5 mM, 20 mL). Under vigorous stirring, freshly prepared $NaBH_4$ solution (224 mM, 2 mL) was added dropwise to the mixture. The resultant mixture was stirred for 30 min and the brown-black Pt NWs colloid solution was obtained. pATP-β-CDP/rGO (20 mg) was added to the excess as-prepared PtNWs under vigorous stirring and these mixtures were sonicated for 10 min. After stirring for an additional 1 h, black suspensions were separated by centrifugation and washed with deionized water for several times, and then dried 24 h in a vacuum drying oven at 60 $^\circ C$.

3. Results and discussion

3.1. Self-assembly of pATP-β-CDP on rGO

Self-assembly process of β-CDP-pATP onto rGO was confirmed by UV–vis absorption spectra. In Fig. 1(a), the characteristic absorption peak of pATP shows at 251 nm and corresponds to $\pi \rightarrow \pi^*$ electron transition of benzene ring. A shoulder peak at 300 nm

Scheme 1. Schematic diagram of the procedure for preparing PtNWs/pATP-β-CDP/rGO.
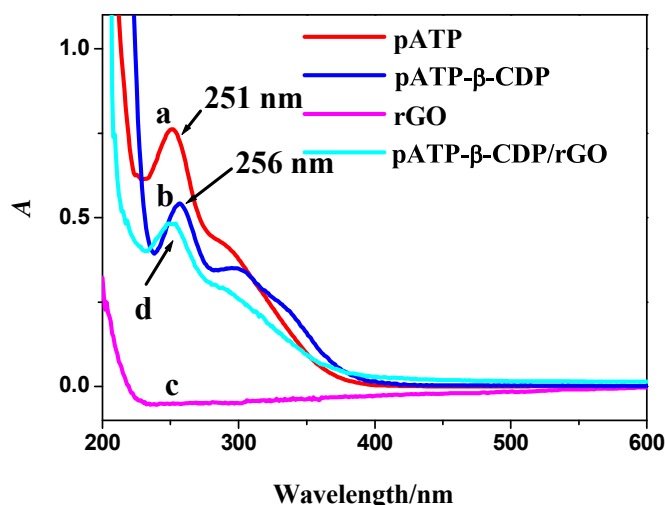
Fig. 1. UV–vis spectra of (a) pATP, (b) pATP-β-CDP, (c) rGO, (d) pATP-β-CDP/rGO.

might be associated with n → π* electron transition. β-CDP has no UV–vis absorption. However, in Fig. 1(b), the characteristic absorption peak in β-CDP-pATP shifts to 256 nm, which indicates that the formation of inclusion complex leads to the red shift of π → π* electron transition. The shoulder peak also displays the slight red shift. Any absorption of rGO is not observed in Fig. 1(c). As a result, in Fig. 1(d), the peak at 251 nm in pATP-β-CDP/rGO is assigned to the absorbance peak of pATP-β-CDP, demonstrating the decoration of pATP-β-CDP on the surface of rGO through non-covalent bond. Compare with polar aqueous solution, these inclusion complexes on the surface of rGO are located at relative nonpolar surroundings, which results in the blue shift of absorbance peak of pATP-β-CDP. Therefore, UV–vis absorption spectra confirm the self-assembly process of β-CDP-pATP onto rGO.

The FTIR spectra of (a) β-CDP, (b) pATP, (c) pATP-β-CDP, (d) rGO, and (e) pATP-β-CDP/rGO were taken by FTIR spectrometer and shown in Fig. 2. For pure β-CDP, in curve a, the bands observed at 3390 cm^{-1} and 2918 cm^{-1} are assigned to −OH stretching vibration and −CH$_2$ asymmetric stretching vibration, respectively. The characteristic band at 1026 cm^{-1} is assigned to the stretching vibration
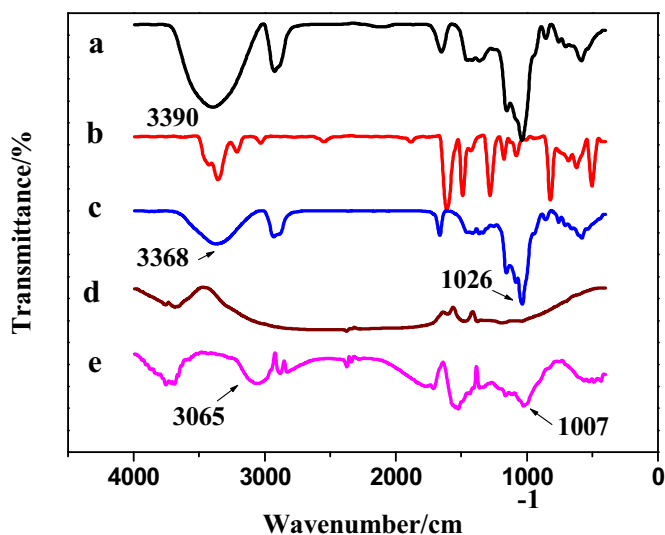
of C−O−C. In Fig. 2(b), for pure pATP, the bands observed at 3433, 3354 and 3210 cm^{-1} are assigned to −NH$_2$ stretching vibration. The bands observed at 1612 cm^{-1} and 1487 cm^{-1} are assigned to the phenyl plane bending vibrations. However, in Fig. 2(c), all characteristic peaks of pATP are not observed in inclusion complexes of pATP-β-CDP. Because pATP molecules enter the hydrophobic cavities of β-CDP, the vibrations of absorption bands of pATP are restrained, which provides a substantial evidence for the formation of pATP-β-CDP inclusion complexes. In Fig. 2(d), the oxygen functional groups in rGO are not shown, indicating the reduction of GO. By comparing FTIR spectra of pATP-β-CDP, rGO and pATP-β-CDP/rGO, it is noted that when rGO is decorated by pATP-β-CDP, the peaks at 3368 cm^{-1} of −OH and 1026 cm^{-1} of C−O−C in pATP-β-CDP stretching vibrations shift to 3065 and 1007 cm^{-1} in pATP-β-CDP/rGO, respectively (Fig. 2(e)). It is identified as a result of hydrogen interactions between hydroxyl groups of β-CDP and some oxygen-containing groups of rGO [31]. The result illustrates that pATP-β-CDP has successfully decorated onto rGO to form pATP-β-CDP/rGO nanocomposites.

3.2. Self-assembly of PtNWs on pATP-β-CDP/rGO

TEM images confirm that PtNWs self-assemble onto rGO to fabricate PtNWs/pATP-β-CDP/rGO composites by using pATP-β-CDP as a linker. Fig. 3 shows the TEM images of PtNWs/pATP-β-CDP/rGO composites prepared with different $\gamma_{IC/G}$: 0.05, 0.1 and 0.5. Obviously, with the increase of $\gamma_{IC/G}$, the density of PtNWs on pATP-β-CDP/rGO increases, which means that the density of PtNWs modified on rGO might be controlled by adjusting the weight ratio of pATP-β-CDP:rGO.

To confirm PtNWs anchoring on the surface of pATP-β-CDP/rGO and the content of PtNWs in the composites, EDX was used to characterize PtNWs/pATP-β-CDP/rGO composites. Fig. 4 is representative EDX spectrum of sample obtained with weight ratio of pATP-β-CDP:rGO = 0.5. EDX spectrum shows that the main elemental compositions of the nanocomposites are Pt, C, N, O and S. The result indicates that both pATP-β-CDP and PtNWs are well-absorbed onto the surface of rGO to fabricate the PtNWs/pATP-β-CDP/rGO nanocomposites. From EDX result, the content of PtNWs in the composites is increased with the weight ratio of pATP-β-CDP:rGO. The contents of PtNWs in the composites are 25.6%, 29.8% and 40.2%, respectively, corresponding to the weight ratio of pATP-β-CDP:rGO 0.05, 0.1 and 0.5. The highest loading amount of PtNWs on PtNWs/pATP-β-CDP/rGO is higher than recently reported GN-T-PtNPs composites [32], which may be attributed to the stronger interaction between PtNWs and mercapto group of pATP than that between PtNPs and amino of amphiphilic calixarene.

Fig. 5 shows XRD patterns of rGO, pATP-β-CDP, pATP-β-CDP/rGO and PtNWs/pATP-β-CDP/rGO. For rGO (curve a), there is a broad feature diffraction peak at about 23.9°. Inclusion complex of pATP-β-CDP displays a typical noncrystal diffraction at 18.7° (curve b). As for pATP-β-CDP on rGO, the diffraction peaks at 19.5° should be the superposition diffraction peak of pATP-β-CDP and rGO (curve c). XRD pattern of the PtNWs/pATP-β-CDP/rGO composite in curve d exhibits diffraction peaks at 2θ = 39.8°, 46.2°, and 67.4° that can be identified as the Pt (111), Pt (200), and Pt (220) reflections of the platinum face-centered cubic crystals [33]. The diffraction peaks at 19.5° should be the superposition diffraction peak of pATP-β-CDP and rGO. XRD patterns also confirm successful preparation of PtNWs/pATP-β-CDP/rGO composite.

The significant structural changes of the graphitic substrate during the synthesis process are present in the Raman spectra (Fig. 6). There are two bands in the Raman spectrum: D band (defects/disorder-induced modes) at 1345 cm^{-1} and G band (in-plane stretching tangential modes) at 1590 cm^{-1} for rGO, pATP-β-CDP/
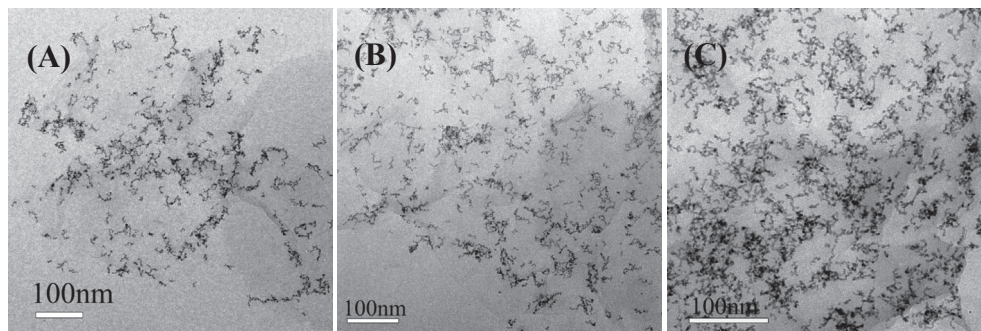

Fig. 2. FT-IR spectra of (a) β-CDP, (b) pATP, (c) pATP-β-CDP, (d) rGO, (e) pATP-β-CDP/rGO.

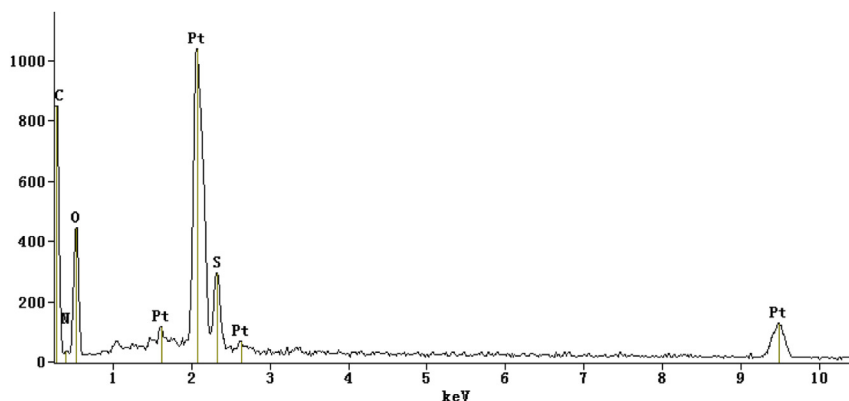**Fig. 3.** TEM images of PtNWs/pATP-β-CDP/rGO with $\gamma_{IC/G}$ of (A) 0.05, (B) 0.1, (C) 0.5.

Fig. 4. EDX spectrum of sample PtNWs/pATP-β-CDP/rGO obtained with weight ratio of pATP-β-CDP:rGO = 0.5.

rGO, and PtNWs/pATP-β-CDP/rGO samples. For the rGO, the intensity ratio (I_D/I_G) is 0.89. As for the pATP-β-CDP/rGO, the intensity ratio (I_D/I_G) increases to 0.99. The increased ratio shows that the number of defects in the rGO increases with pATP-β-CDP self-assembling onto the rGO. The intensity ratio (I_D/I_G) is 1.00 for PtNWs/pATP-β-CDP/rGO and no noticeable change compared to pATP-β-CDP/rGO.

TGA was used to determine the loading amount of PtNWs on the surface of rGO. Fig. 7 shows the weight losses of rGO (curve a),

pATP-β-CDP (curve b), pATP-β-CDP/rGO (curve c), PtNWs (curve d) and PtNWs/pATP-β-CDP/rGO (curve e). rGO shows much higher thermal stability with only a mass loss of 8.5% up to 600 °C. For pATP-β-CDP (curve b), two main steps of weight loss shown in curve b are observed. The first step ranging from 35 to 105 °C is due to the loss of moisture. The second weight loss ranging from 300 to 400 °C is assigned to the decomposed of pATP-β-CDP. From the weight loss ratio of rGO (curve a), pATP-β-CDP (curve b) and pATP-β-CDP/rGO (curve c), the amount of pATP-β-CDP molecules
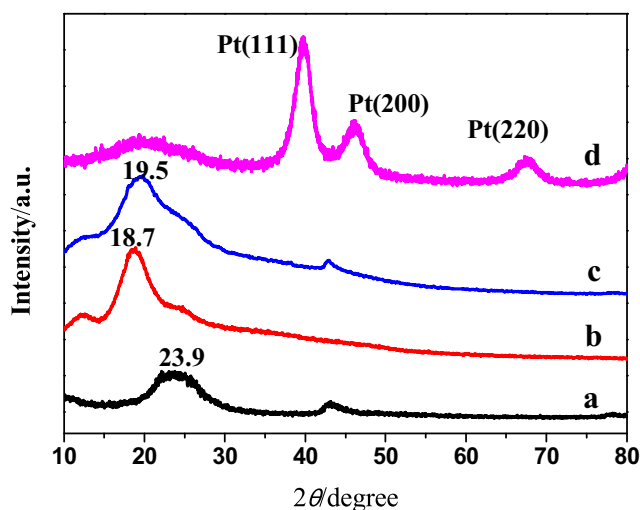

Fig. 5. XRD patterns of (a) rGO, (b) pATP-β-CDP, (c) pATP-β-CDP/rGO, (d) PtNWs/pATP-β-CDP/rGO.
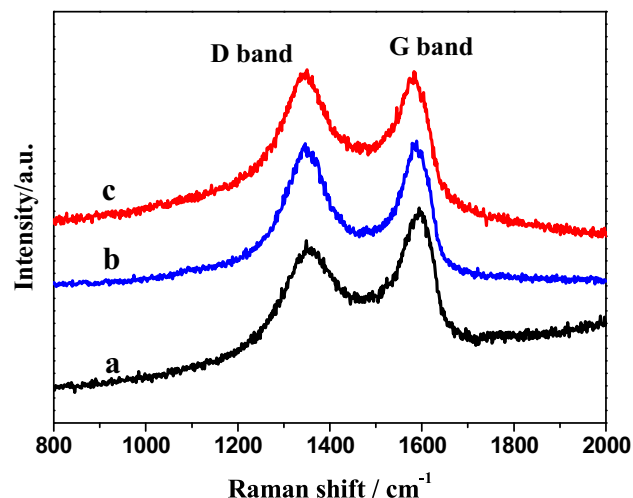

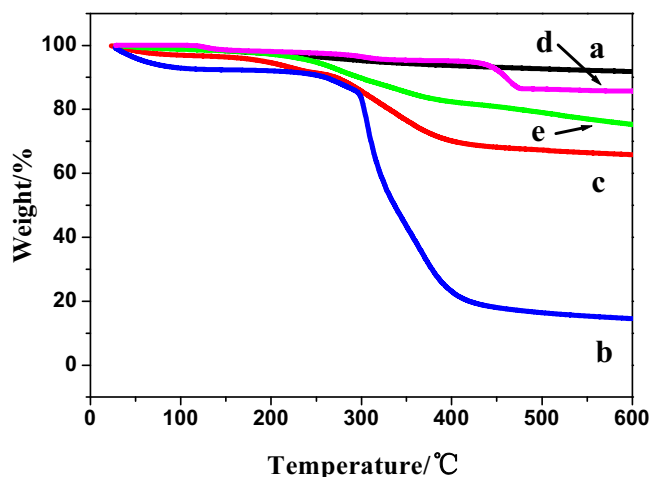**Fig. 6.** Raman spectra of (a) rGO, (b) pATP-β-CDP/rGO, (c) PtNWs/pATP-β-CDP/rGO.

Fig. 7. TGA of (a) rGO, (b) pATP-β-CDP, (c) pATP-β-CDP/rGO, (d) PtNWs, (e) PtNWs/pATP-β-CDP/rGO.

adsorbed on the surface of rGO might be calculated from the following equation.

$$\frac{m_{rGO} \times a\% + m_{pATP-\beta-CDP} \times b\%}{m_{rGO} + m_{pATP-\beta-CDP}} \times 100\% = c\% \quad (1)$$

Where $a\%$, $b\%$ and $c\%$ are the weight loss ratio of rGO, pATP-β-CDP and pATP-β-CDP/rGO, respectively. m_{rGO} and $m_{pATP-\beta-CDP}$ are the mass of rGO and pATP-β-CDP in the pATP-β-CDP/rGO nanocomposites. From above equation, m_{rGO}: $m_{pATP-\beta-CDP}$ is 2.1 and the amount of pATP-β-CDP molecules adsorbed on the surface of rGO is about 32%.

As to the PtNWs/pATP-β-CDP/rGO (curve e), the weight loss is attributed to the decomposition of pATP-β-CDP, rGO and capping ligands on PtNWs. From the weight loss ratio of rGO (curve a), pATP-β-CDP (curve b) and PtNWs (curve d), the amount of PtNWs self-assembling on the surface of pATP-β-CDP/rGO might be calculated from the Eq. (2).

$$\frac{m'_{rGO} \times a\% + m'_{pATP-\beta-CDP} \times b\% + m_{PtNWs} \times d\%}{m'_{rGO} + m'_{pATP-\beta-CDP} + m_{PtNWs}} \times 100\% = e\%$$

(2)

Where $d\%$ and $e\%$ are the weight loss ratio of PtNWs and PtNWs/pATP-β-CDP/rGO, respectively. m'_{rGO}, $m'_{pATP-\beta-CDP}$ and m_{PtNWs} are the mass of rGO, pATP-β-CDP and PtNWs in the PtNWs/pATP-β-CDP/rGO nanocomposites, respectively. According to m_{rGO}: $m_{pATP-\beta-CDP}$ and Eq. (2), $(m_{rGO} + m_{pATP-\beta-CDP})$: m_{PtNWs} is 1.35 and the amount of PtNWs self-assembling on the surface of pATP-β-CDP/rGO is 42.5%, which is close to the value obtained by EDX.

A reversible precipitation–dispersion behavior further confirms the dispersibility and stability of PtNWs/pATP-β-CDP/rGO hybrids. Black precipitations of PtNWs/pATP-β-CDP/rGO may be dispersed into aqueous solution to form homogeneous suspensions by vigorous hand-shaking. This is very important to manipulate the metal nanoparticles/GN hybrid materials for practical applications. More importantly, by means of the connection of thiol and amino groups of pATP, this method is also suitable to assemble other noble metal nanopartilces on the surface of β-CDP-pATP/rGO to form metal nanopartilces/rGO hybrid materials.

3.3. Electrocatalytic oxidation of methanol on PtNWs/pATP-β-CDP/rGO

The electrochemical active surface areas of PtNWs/pATP-β-CDP/rGO and commercial Pt/C catalyst were determined by the voltammetric measurements at a scanning rate of 50 mV s^{-1} in 0.5 M H$_2$SO$_4$ of saturated nitrogen. In Fig. 8, curve a shows the typical multiple peaks in the lower potential range of −0.2 to 0 V, which are related to hydrogen reductive adsorption/oxidative desorption on a Pt surface [34]. The anodic peak at the higher potential around 0.8 V and its cathodic counterpart at about 0.55 V are due to the formation and reduction of the Pt oxide monolayer [35]. The electrochemical active surface area (ECSA) is estimated by integrating the voltammogram corresponding to the hydrogen desorption from the electrode surface after deduction of the double-layer region. The ECSA for PtNWs/pATP-β-CDP/rGO and Pt/C catalysts are 64.5 and 21.4 m^2 g^{-1}, respectively. Higher ECSA of PtNWs/pATP-β-CDP/rGO is favorable to electrocatalytic activity for methanol.

The electrocatalytic performances of bare GCE, pATP-β-CDP/rGO, rGO, PtNWs/pATP-β-CDP/rGO and Pt/C for methanol oxidation were investigated in a 0.5 M H$_2$SO$_4$ solution containing 2.0 M CH$_3$OH. As shown in Fig. 9(A), the bare GCE (curve a), pATP-β-CDP/rGO (curve b) and rGO (curve c) do not show electrocatalytic activity toward the oxidation of methanol. However, PtNWs/pATP-β-CDP/rGO (curve e) exhibits very high peak current for the oxidation of methanol. It is obvious that the catalytic performance of PtNWs/pATP-β-CDP/rGO is superior to that of Pt/C, which is attributed to the higher ECSA of PtNWs/pATP-β-CDP/rGO. The typical methanol oxidation current peak on the Pt catalyst is at approximately 0.67 V versus SCE in the forward scan. In most of the literature, the typical methanol oxidation current peak on the Pt catalyst is at approximately 0.74 V versus SCE in the anodic scan [15,36,37]. A lower anodic over potential of PtNWs/pATP-β-CDP/rGO demonstrates higher electrocatalytic activity. Additionally, the ratio of the forward oxidation current peak (I_f) to the reverse current peak (I_b), I_f/I_b, is an important index of the catalyst tolerance to the poisoning species, Pt=C=O [36]. A higher ratio indicates more effective removal of the poisoning species on the catalyst surface. As shown in Fig. 9(A), the I_f/I_b ratio of PtNWs/pATP-β-CDP/rGO is 1.56, which is higher than that of Pt/C (I_f/I_b 1.08). Compared with recent state-of-art Pt-based carbon materials such as Pt/carbon nanofiber (<1.0) [15], Pt/CNT composite (0.88) [36], the platinum
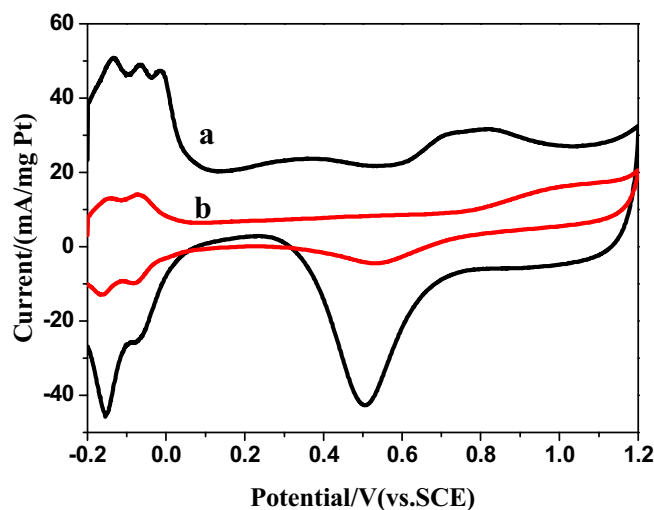

Fig. 8. Voltammograms of (a) PtNWs/pATP-β-CDP/rGO and (b) commercial Pt/C catalyst in 0.5 M H$_2$SO$_4$ with scan rate of 50 mV s^{-1}.
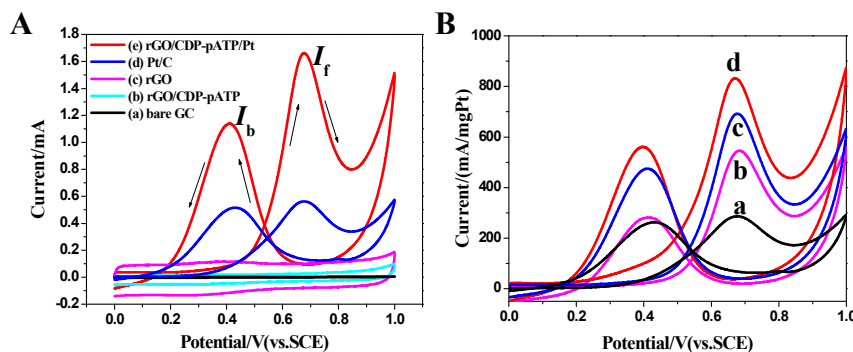
Fig. 9. (A) Voltammograms of the catalytic oxidation of methanol on (a) bare GCE, (b) pATP-β-CDP/rGO, (c) rGO, (d) Pt/C, (e) PtNWs/pATP-β-CDP/rGO in 0.5 M H_2SO_4 solution containing 2.0 M methanol. (B) Voltammograms of the catalytic oxidation of methanol on (a) Pt/C and PtNWs/pATP-β-CDP/rGO obtained with different weight ratio of pATP-β-CDP:rGO: (b) 0.05, (c) 0.1, (d) 0.5. *Y*-axis: the electrocatalytic current is normalized to Pt-loading. Scan rate: 50 mV s^{-1}.

black (0.95) [38], commercial E-TEK Pt/C catalysts (0.70) [38], and GN/Pt NP hybrids (1.25) [38], PtNWs/pATP-β-CDP/rGO shows better catalyst tolerance, which is conductive to improve the electro-catalytic cycling stabilities.

The mass current density for CH_3OH oxidation may accurately reflect the performance of catalyst. Fig. 9(B) clearly shows that the PtNWs/pATP-β-CDP/rGO obtained with different weight ratio of pATP-β-CDP:rGO are used to catalyze the CH_3OH oxidation. It is clear that PtNWs/pATP-β-CDP/rGO catalyst obtained with weight ratio of pATP-β-CDP:rGO = 0.5 displays the highest mass current density. Commercial Pt/C modified electrode shows the smallest mass current density for CH_3OH oxidation. The mass current density for 1 M methanol oxidation on PtNWs/pATP-β-CDP/rGO is 590 mA mg^{-1} Pt. The mass current density of PtNWs/pATP-β-CDP/rGO is much higher recent state-of-art Pt-based nanomaterials, such as Pt/MWCNT-10nm catalyst (429.8 mA mg^{-1} Pt) [39], 60 wt % Pt/GS (246.7 mA mg^{-1} Pt) [40], and Pt/MWCNT composite (160 mA mg^{-1} Pt) [41] (indexing 1 M methanol). Higher activity in electrochemical performance is probably ascribed to the high level of dispersion of PtNWs on the surface of rGO and the outstanding water-dispersible performance of PtNWs/pATP-β-CDP/rGO. Actually, some Pt-alloy materials, such as PtRu/MnO$_2$/CNTs [42], Pt-WC/RGO [43], Pt-on-Pd bimetallic nanodendrites (TP-BNGN) [38] and FePtPd Nanowires [44] would exhibit the higher the mass current density due to the low content of Pt in the alloy materials.

Fig. 10(A) shows the effect scanning rates on CVs of the PtNWs/pATP-β-CDP/rGO modified electrode in a solution containing 0.5 M H_2SO_4 and 2.0 M methanol. The peak currents increase with the increasing scan rates. The forward oxidation peak current versus

the square root of sweep rates is shown in Fig. 10(B), in which a straight line with correlation coefficient of 0.996 is obtained, indi-cating that the oxidation of methanol on the PtNWs/pATP-β-CDP/rGO modified electrode is controlled by mass transfer.

Fig. 11(A) shows the correlation of methanol oxidation at PtNWs/pATP-β-CDP/rGO modified electrode as a function of methanol concentration. The forward oxidation peak current in-creases significantly with increasing methanol concentrations from 0.3 to 4.0 M. As shown in Fig. 11(B), the calibration plot further confirms a good linear relationship between the forward oxidation current and the concentrations of methanol, which indicates that the methanol oxidation reaction is well-controlled by the methanol concentration at PtNWs/pATP-β-CDP/rGO surface.

The long-term electrocatalytic stabilities of PtNWs/pATP-β-CDP/rGO and commercial Pt/C were compared in 0.5 M H_2SO_4 solution containing 2.0 M methanol using chronoamperometry and cyclic voltammetry. In Fig. 12(A), chronoamperometric measurements at potentials 0.6 V for 1 h were carried out. At a fixed potential, the intermediate products such as carbon monoxide would adsorb and accumulate on the electrode surface due to the methanol oxidation, which might lead to the catalysts inactivation and the rapid current attenuation [37,45]. As shown in Fig. 12(A), the oxidation current on commercial Pt/C modified electrode decreases much more rapidly than that on PtNWs/pATP-β-CDP/rGO modified electrode at the initial stage. Then the currents on two modified electrodes gradu-ally decay and achieve a pseudo-steady state. Obviously, the PtNWs/pATP-β-CDP/rGO catalyst retains a higher current than commercial Pt/C for the whole time. This result confirms that PtNWs/pATP-β-CDP/rGO catalyst has the higher poison tolerance
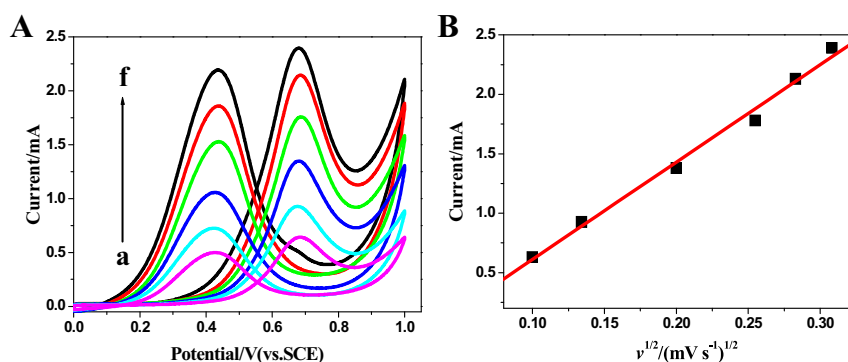

Fig. 10. (A) Cyclic voltammograms of 2.0 M methanol on PtNWs/pATP-β-CDP/rGO modified electrode at various scan rates in 0.5 M H_2SO_4 solution. Scan rates (mV s^{-1}): (a) 10, (b) 20, (c) 40, (d) 60, (e) 80, (f) 100. (B) Plot of the forward oxidation peak current versus square root of sweep rate.
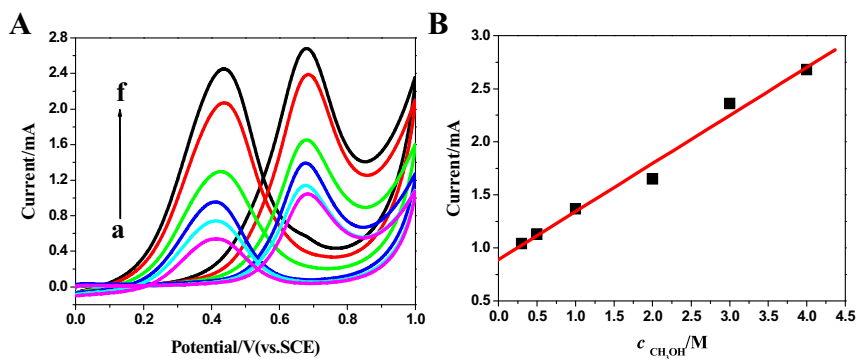
Fig. 11. (A) Cyclic voltammograms of different concentrations of methanol on PtNWs/pATP-β-CDP/rGO modified electrode at 50 mV s^{-1} in 0.5 M H$_2$SO$_4$ solution. c_{CH3OH}/M: (a) 0.3, (b) 0.5, (c) 1, (d) 2, (e) 3, (f) 4. (B) Plot of the forward oxidation peak current versus concentrations of methanol.
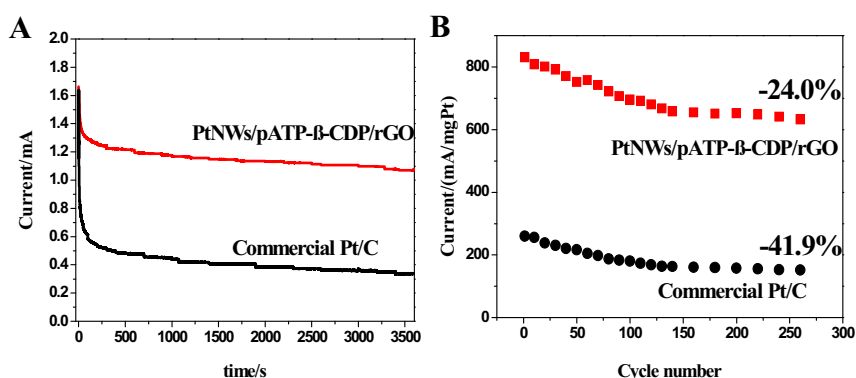

Fig. 12. Electrocatalytic cycling stability of PtNWs/pATP-β-CDP/rGO catalyst and commercial Pt/C. (A) Chronoamperometric response recorded at 0.6 V (vs. SCE) in 0.5 M H$_2$SO$_4$ and 2 M methanol solution. (B) Cyclic voltammograms recorded 260 cycles in 0.5 M H$_2$SO$_4$ and 2 M methanol solution.

and better electrochemical stability than commercial Pt/C. The strong interaction between Pt atoms and thiol groups of pATP weakens CO adsorption and enhances CO tolerance [46]. The electrocatalytic cycling stabilities of the PtNWs/pATP-β-CDP/rGO and commercial Pt/C in 0.5 M H$_2$SO$_4$ solution containing 2.0 M methanol have also been investigated using CV cycling, as shown in Fig. 12(B). It can be observed that the forward peak current density for methanol oxidation on PtNWs/pATP-β-CDP/rGO modified electrode decreases by about 24.0% within the 260 scans. However, the peak current density on commercial Pt/C modified electrode declines about 41.9% in the same scans. The good cycling stabilities may be attributed to the strong interaction between PtNWs and thiol groups, which enhances CO tolerance, results in the stable assembly and the favorable dispersion of PtNWs on the surface of rGO and avoids the rapid current decay during the long time CV cycling.

4. Conclusions

In conclusion, we have developed a new strategy to realize the self-assembly of Pt nanoworms on rGN through inclusion complex-pATP-β-CDP. Through the self-assembly strategy, the amount of PtNWs and the dispersity on rGO could be adjusted by changing the weight ratio of pATP-β-CDP:rGO. Novel hybrid catalyst PtNWs/pATP-β-CDP/rGO is found to have better electrocatalytic activity and cycling stability towards methanol oxidation reaction in acid solution than commercial Pt/C catalyst. The excellent catalytic properties of rGO hybrid materials offer the potential application for catalyst of fuel cell.

References

[1] S. Wasmus, A. Küver, J. Electroanal. Chem. 461 (1999) 14–31.
[2] A.S. Aricò, S. Srinivasan, V. Antonucci, Fuel Cells 1 (2001) 133–161.
[3] H. Liu, C. Song, L. Zhang, J. Zhang, H. Wang, D.P. Wilkinson, J. Power Sources 155 (2006) 95–110.
[4] K.-W. Park, J.-H. Choi, B.-K. Kwon, S.-A. Lee, Y.-E. Sung, H.-Y. Ha, S.-A. Hong, H. Kim, A. Wieckowski, J. Phys. Chem. B 106 (2002) 1869–1877.
[5] Z. Liu, X.Y. Ling, X. Su, J.Y. Lee, J. Phys. Chem. B 108 (2004) 8234–8240.
[6] X. Chen, Z. Cai, X. Chen, M. Oyama, Carbon 66 (2014) 387–394.
[7] Y. Shao, J. Liu, Y. Wang, Y. Lin, J. Mater. Chem. 19 (2008) 46–59.
[8] Y.L. Hsin, K.C. Hwang, C.-T. Yeh, J. Am. Chem. Soc. 129 (2007) 9999–10010.
[9] L. Li, Y. Xing, J. Phys. Chem. C 111 (2007) 2803–2808.
[10] M.-Y. Duan, R. Liang, N. Tian, Y.-J. Li, E.S. Yeung, Electrochim. Acta 87 (2013) 432–437.
[11] M. Pan, H. Tang, S.P. Jiang, Z. Liu, J. Electrochem. Soc. 152 (2005) A1081–A1088.
[12] S. Zhang, Y. Shao, G. Yin, Y. Lin, J. Mater. Chem. 20 (2010) 2826–2830.
[13] L. Li, J. Zhang, Y. Liu, W. Zhang, H. Yang, J. Chen, Q. Xu, ACS Sustain. Chem. Eng. 1 (2013) 527–533.
[14] M. Kosaka, S. Kuroshima, K. Kobayashi, S. Sekino, T. Ichihashi, S. Nakamura, T. Yoshitake, Y. Kubo, J. Phys. Chem. C 113 (2009) 8660–8667.

[15] D. Wang, Y. Liu, J. Huang, T. You, J. Colloid Interface Sci. 367 (2012) 199—203.
[16] K. Kwon, Y.J. Sa, J.Y. Cheon, S.H. Joo, Langmuir 28 (2012) 991—996.
[17] J.H. Kim, B. Fang, S.B. Yoon, J.-S. Yu, Appl. Catal. B Environ. 88 (2009) 368—375.
[18] J. Zang, L. Dong, Y. Jia, H. Pan, Z. Gao, Y. Wang, Appl. Catal. B Environ. 144 (2014) 166—173.
[19] A.H. Castro Neto, F. Guinea, N.M.R. Peres, K.S. Novoselov, A.K. Geim, Rev. Mod. Phys. 81 (2009) 109—162.
[20] A.A. Balandin, S. Ghosh, W. Bao, I. Calizo, D. Teweldebrhan, F. Miao, C.N. Lau, Nano Lett. 8 (2008) 902—907.
[21] A.C. Ferrari, J.C. Meyer, V. Scardaci, C. Casiraghi, M. Lazzeri, F. Mauri, S. Piscanec, D. Jiang, K.S. Novoselov, S. Roth, A.K. Geim, Phys. Rev. Lett. 97 (2006) 187401.
[22] X. Li, X. Wang, L. Zhang, S. Lee, H. Dai, Science 319 (2008) 1229—1232.
[23] S. Stankovich, D.A. Dikin, G.H.B. Dommett, K.M. Kohlhaas, E.J. Zimney, E.A. Stach, R.D. Piner, S.T. Nguyen, R.S. Ruoff, Nature 442 (2006) 282—286.
[24] Y. Li, L. Tang, J. Li, Electrochem. Commun. 11 (2009) 846—849.
[25] Y. Li, W. Gao, L. Ci, C. Wang, P.M. Ajayan, Carbon 48 (2010) 1124—1130.
[26] Y.-G. Zhou, J.-J. Chen, F. Wang, Z.-H. Sheng, X.-H. Xia, Chem. Commun. 46 (2010) 5951—5953.
[27] F. Li, Y. Guo, Y. Liu, H. Qiu, X. Sun, W. Wang, Y. Liu, J. Gao, Carbon 64 (2013) 11—19.
[28] S.C. Sahu, A.K. Samantara, B. Satpati, S. Bhattacharjee, B.K. Jena, Nanoscale 5 (2013) 11265—11274.
[29] W. Zhang, M. Chen, G. Diao, Electrochim. Acta 56 (2011) 5129—5136.
[30] M. Chen, J. Wang, W. Zhang, G. Diao, J. Electroanal. Chem. 696 (2013) 1—8.
[31] Y. Guo, S. Guo, J. Ren, Y. Zhai, S. Dong, E. Wang, ACS Nano 4 (2010) 4001—4010.
[32] J. Zhou, M. Chen, G. Diao, J. Mater. Chem. A 1 (2013) 2278—2285.
[33] Z. Yan, M. Zhang, J. Xie, H. Wang, W. Wei, J. Power Sources 243 (2013) 48—53.
[34] H. Razmi, E. Habibi, J. Solid State Electrochem. 13 (2009) 1897—1904.
[35] C. Paoletti, A. Cemmi, L. Giorgi, R. Giorgi, L. Pilloni, E. Serra, M. Pasquali, J. Power Sources 183 (2008) 84—91.
[36] Y. Mu, H. Liang, J. Hu, L. Jiang, L. Wan, J. Phys. Chem. B 109 (2005) 22212—22216.
[37] H. Huang, D. Sun, X. Wang, J. Phys. Chem. C 115 (2011) 19405—19412.
[38] S. Guo, S. Dong, E. Wang, ACS Nano 4 (2010) 547—555.
[39] Z.Q. Tian, S.P. Jiang, Y.M. Liang, P.K. Shen, J. Phys. Chem. B 110 (2006) 5343—5350.
[40] J. Zhao, H. Yu, Z. Liu, M. Ji, L. Zhang, G. Sun, J. Phys. Chem. C 118 (2014) 1182—1190.
[41] S.-F. Zheng, J.-S. Hu, L.-S. Zhong, L.-J. Wan, W.-G. Song, J. Phys. Chem. C 111 (2007) 11174—11179.
[42] C. Zhou, F. Peng, H. Wang, H. Yu, C. Peng, J. Yang, Electrochem. Commun. 12 (2010) 1210—1213.
[43] C. Ma, W. Liu, M. Shi, X. Lang, Y. Chu, Z. Chen, D. Zhao, W. Lin, C. Hardacre, Electrochim. Acta 114 (2013) 133—141.
[44] S. Guo, S. Zhang, X. Sun, S. Sun, J. Am. Chem. Soc. 133 (2011) 15354—15357.
[45] B. Liu, J.H. Chen, C.H. Xiao, K.Z. Cui, L. Yang, H.L. Pang, Y.F. Kuang, Energy Fuels 21 (2007) 1365—1369.
[46] L. Guo, S. Chen, L. Li, Z. Wei, J. Power Sources 247 (2014) 360—364.